DOUBLE NUCLEUS IN M83

Damián Mast,[1] Rubén J. Díaz,[1,2] and M. Paz Agüero[1]

ABSTRACT

M83 is one of the nearest galaxies with enhanced nuclear star formation, and it presents one of the best opportunities to study the kinematics and physical properties of a circumnuclear starburst. Our three-dimensional spectroscopy data in the R band confirm the presence of a secondary nucleus or mass concentration (previously suggested by Thatte and coworkers). We determine the position of this hidden nucleus, which would be more massive than the visible one and was not detected in the optical *Hubble Space Telescope* images due, probably, to the strong dust extinction. Using a Keplerian approximation, we estimated for the optical nucleus a mass of $(5.0 \pm 0.8) \times 10^6\ M_\odot / \sin i\ (r < 1\farcs5)$, and for the hidden nucleus, located $4'' \pm 1''$ to the northwest (position angle of $271° \pm 15°$) of the optical nucleus, a mass of $(1.00 \pm 0.08) \times 10^7\ M_\odot / \sin i\ (r < 1\farcs5)$. The emission-line ratio map also unveils the presence of a second circumnuclear ring structure, previously discovered by IR imaging (Elmegreen and coworkers). The data allow us to resolve the behavior of the interstellar medium inside the circumnuclear ring and around the binary mass concentration.

Key words: galaxies: individual (M83) — galaxies: kinematics and dynamics — galaxies: nuclei — galaxies: starburst — galaxies: structure — techniques: spectroscopic

1. INTRODUCTION

M83 is a very special case of nearby grand design barred spiral galaxies (Table 1); it harbors a nuclear X-ray source (Soria & Wu 2003), coexisting with a massive starburst in a double circumnuclear ring (Elmegreen et al. 1998) and a secondary mass concentration recently suggested by Thatte et al. (2000) and confirmed by three-dimensional spectroscopic data (Mast et al. 2002). Gallais et al. (1991) obtained IR images of the central $20''$ in the J, H, and K bands and analyzed the color-color diagrams, which indicate that the nucleus and several regions in an arc at $7''$ from the nucleus are forming stars at a high rate. *Hubble Space Telescope* (*HST*) observations (optical and UV) and *IUE* spectra reveal that the arc contains more than 20 massive young clusters, similar to 30 Dor in the Large Magellanic Cloud (LMC), with ages between 2 and 8 million years and masses in the range 1×10^4–$1 \times 10^6\ M_\odot$ (Heap et al. 1993; Heap 1994).

Thatte et al. (2000) made IR spectroscopic observations with two long-slit positions of the nuclear region using the ISAAC spectrometer at the Very Large Telescope. They detected two peaks in the radial velocity dispersion profile, one on the K-band luminosity peak and the other one displaced about $3''$ to the southwest, suggesting the presence of a secondary nucleus. The lack of two spatial dimensions in the spectroscopic information did not allow them to fix the precise position of the second mass concentration. Although the morphology of the star formation activity has been studied in detail (Gallais et al. 1991; Harris et al. 2001), there are very few kinematic or dynamical studies based on good spatial samplings. In this work we present a study of the two-dimensional kinematics of the central region of this galaxy, which resolves the behavior of the interstellar medium around the binary mass concentration.

2. OBSERVATIONS

A summary of the observations is presented in Table 2. We made three-dimensional spectroscopic observations of the central region of M83 using the Multifunctional Integral Field Spectrograph mounted on the 1.54 m telescope at Bosque Alegre Astrophysical Station (Díaz et al. 1999, 2003). The data were gathered between 2001 March and 2002 May. Several circumnuclear fields were observed; we present here the analysis of the selected field that includes both mass concentrations.

The analyzed integral field was obtained with a total exposure time of 2 hr. The spectra, with a resolution of 1.5 Å in the R band, were obtained with an array of 8×14 lenses ($1\farcs5$ field each), sampling a field of $12'' \times 21''$. The seeing was about $2''$, so the field is slightly subsampled. We complemented these data with archival *HST* images in filters F187N, F190N (Paα and Paα continuum), F814W (7940 Å), and F656N (6563 Å).

3. DATA REDUCTION AND ANALYSIS

The reduction of the spectra was performed with the software SAO (developed by the Special Astrophysical Observatory, Russia), the software ADHOC (Boulesteix 1993), and PC standard worksheets. The procedure followed is described in detail in the works of Díaz et al. (1997), Vega (2000), Vega et al. (2000), and Mast (2002). The spectra include the nebular emission lines Hα, [N II] $\lambda6548$, $\lambda6583$, and [S II] $\lambda6716$, $\lambda6731$, which were fitted using Gaussian curves to determine the parameters that describe them. In most of the field, the signal-to-noise ratio (S/N) allowed the detection and fitting of the mentioned emission lines, but in some locations (in the field southwest border) the S/N of the spectrum was low, and only Hα and [N II] $\lambda6583$ emission were detected. We performed Gaussian fitting up to a level of 20% of the peak value. Therein, the profile wing asymmetries that in some locations could appear did not strongly affect the manual interactive fitting performed on the lines. Once the emission-line Gaussian fitting was completed, we obtained the following data for each lens: Hα, [N II] $\lambda6583$, [S II] $\lambda6717$, and [S II] $\lambda6731$ fluxes, wavelength positions, and the FWHM of each

[1] Observatorio Astronómico de Córdoba y CONICET, Universidad Nacional de Córdoba, Laprida 854, 5000 Cordoba, Argentina; damian@mail.oac.uncor.edu.
[2] Gemini Observatory, Southern Operations Center, c/o AURA, La Serena, Chile.

TABLE 1
M83 Characteristics

Feature	Value	Reference
$V_\odot$ (km s^{-1})................................	503	1
M..	−20.4	1
Size[a]......................................	12.9×11.5	1
B_T[a] (mag)................................	8.20	2
D ($h = 0.75$) (Mpc)......................	3.7	2
Kinematic major axis, P.A. (deg).............	46	3
i (deg)...................................	24	4
Inner CN ring radius (arcsec)..............	2.8	5
Inner CN ring radius (pc).................	51	5
Outer CN ring radius (arcsec)..............	8.6	5
Outer CN ring radius (pc).................	152	5
Bar length (arcsec).......................	354	6
Bar length (pc)..........................	6	6

[a] Measured at $\mu_B = 25$ mag arcsec^{-2}.

References.—(1) Oddone 1999; (2) de Vaucouleurs et al. 1991; (3) Lundgren et al. 2004; (4) Comte 1981; (5) Elmegreen et al. 1998; (6) Digitized Sky Survey image.

line. With this information the following maps were constructed: red continuum intensity, Hα intensity, [N II] $\lambda6583$/Hα, ([S II] $\lambda6717$ + [S II] $\lambda6731$)/Hα, [S II] $\lambda6717$/[S II] $\lambda6731$, and FWHM maps. Because the Hα line is the most conspicuous emission of the obtained spectra and the one showing the best S/N, we only analyzed the radial velocities corresponding to this line. A map of the radial velocity field was also constructed.

As mentioned before, the field was slightly subsampled. In order to improve the data processing and visualization, all the field values were interpolated, yielding the same field sampled by 24×42 elements (0″5 pixel^{-1}). The internal error due to the velocity determination procedure has a relative value lower than 5 km s^{-1} (rms). That is the precision limit in the velocity field determination, in case we have data with good S/N (>10). In our case the best S/N in the Hα emission line is (S/N)$_{tot}$= 30, (S/N)$_{peak}$ = 15; the worst S/N, in one of the outermost lenses, is (S/N)$_{peak}$ = 2.

4. RESULTS

4.1. Morphological Scenario

Figure 1 shows the central $40'' \times 40''$ around the optical nucleus, from which a bright small red arc emerges to the southwest, but the most conspicuous feature is a giant star-forming arc (Gallais et al. 1991; Elmegreen et al. 1998). In this figure, to the northeast of the nucleus several star clusters are present and have been studied by Harris et al. (2001). Going counterclockwise through the arc, a highly obscured region is seen, with a large number of dust patches and a star-forming region emerging from

the dust more than $5''$ westward from the nucleus. The R-band continuum map (Fig. 2) shows an ellipsoidal light distribution with the external isophotes center, determined from the red continuum HST image (F814W filter), located 2″5 to the west-southwest of the continuum emission peak (position angle [P.A.] of 230°), which we assume corresponds to the optical nucleus position. This result is consistent with the observations of Thatte et al. (2000), who found that the nucleus is not located at the symmetry center (of the circumnuclear light distribution) in their K-band images. The symmetry center of the outer isophotes in the R and K bands, which could be considered the bulge center, is almost the same, implying that the optical nucleus would be not located at the stellar bulge center (see the sketch in Fig. 3).

4.2. Radial Velocity Field of the Ionized Gas

Figure 4 shows the obtained velocity field, which covers $12'' \times 21''$ of the central region of M83. The square marks the position of the optical nucleus, which corresponds to the continuum image peak (in the R band, N_R in Figs. 3 and 4). The isovelocity lines were traced in steps of 10 km s^{-1} (2 σ uncertainty). The isovelocity lines are strongly distorted and could indicate a departure from the axisymmetric potential, with a line crowding at the position indicated by the circle, where the hidden nucleus should be located. The radial velocity field has a distortion that indicates the presence of two mass concentrations, neither of them located exactly on the global velocity field minor axis (Figs. 4 and 7, *dotted line*).

The radial velocity field is similar to that of the central region of NGC 3227 (Arribas & Mediavilla 1994), which shows an active galactic nucleus not at the kinematic center of the galaxy. A previous clear case of a kinematic center not located at the bar + bulge center of symmetry was found by Díaz et al. (1999) in the two-dimensional spectroscopic maps and images of NGC 1672, a southern barred galaxy with a strong circumnuclear starburst.

The extreme velocity values of the observed field are $V_{max} = 634$ km s^{-1} and $V_{min} = 542$ km s^{-1} ($\Delta V = 92$ km s^{-1}). There is an isovelocity line stretching (Fig. 5) that is coincident, within the uncertainties, with the continuum peak previously identified with the optical nucleus, and therefore is about 2″5 to the north-northeast of the red continuum symmetry center (C_R in Figs. 3 and 4). The radial velocity gradient determined by the line stretching indicates that the mass concentration of the hidden nucleus would be larger than that of the visible one.

Areas with predominant circular motion can be drawn around each mass concentration (see Fig. 6). Each area involves 6 lenses (optical nucleus) and 11 lenses (hidden nucleus). The mass concentration corresponding to the optical nucleus and, within the uncertainties, coincident with the continuum peak position is 2″3 ± 0″5 to the west-southwest of the red continuum symmetry center, while the hidden nucleus, kinematically determined, would

TABLE 2
Log of Observations

| Instrument	Date	Exposure Time (s)	λ_0 (Å)	$\Delta\lambda$ (Å)	P.A. (deg)	Pixel Scale	Field of view (arcsec)	Comments
HST	2000 May	600	6563	21	209	0″049	160×160	Hα image
HST	2000 Apr	160	7940	1531	209	0″049	160×160	Red continuum image
HST	1999 May	160	18739	187	212	0″075	19.2×19.2	Paα image
BAlegre[a].........	2002 May	3600	6600	800	96	1″5, 0.78 Å	12×21	Integral field
BAlegre[a].........	2002 May	3600	6600	800	96	1″5, 0.78 Å	12×21	Integral field

[a] Estación Astrofísica de Bosque Alegre.
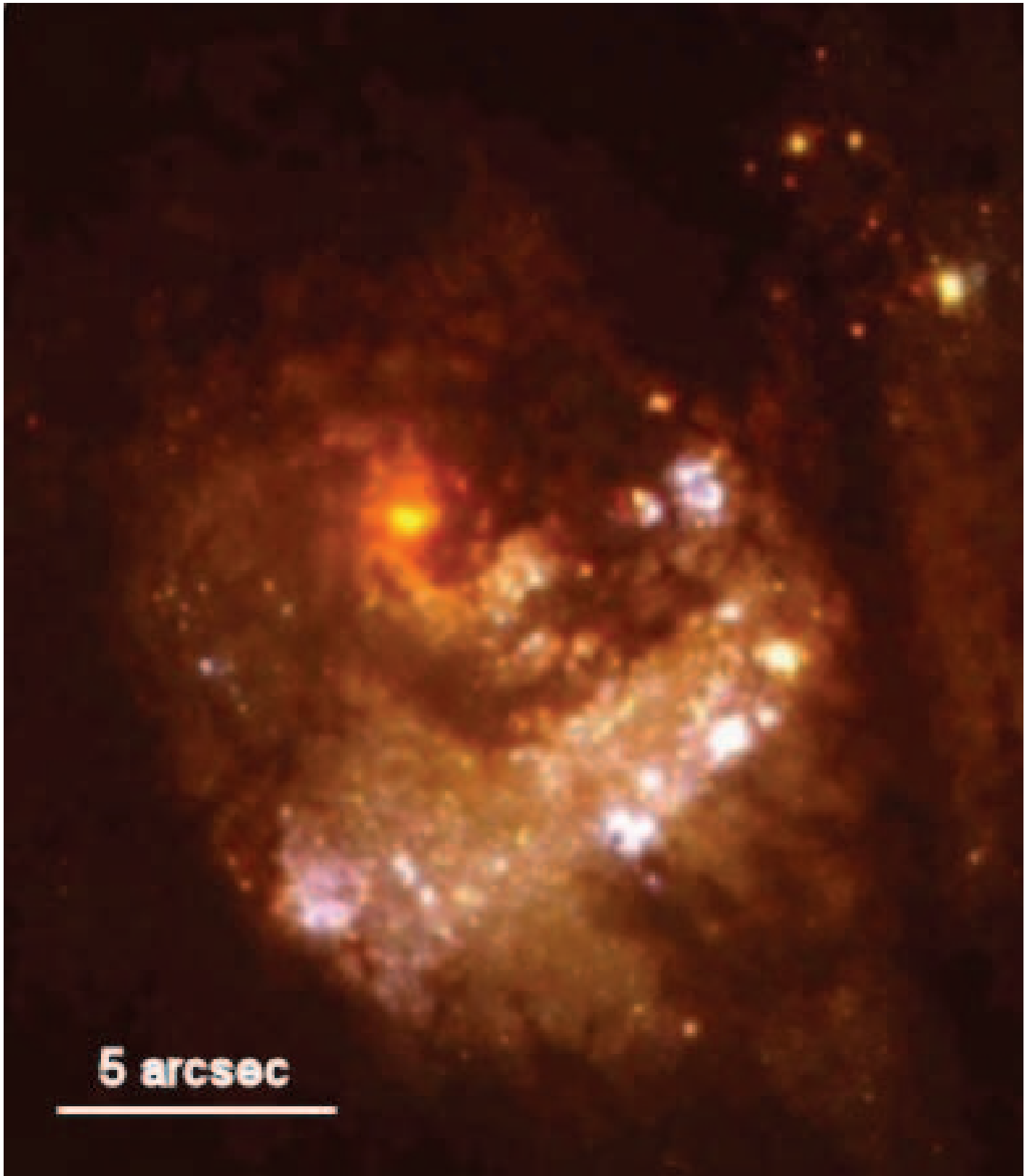
Fig. 1.—*HST* false-color image combined from F439W (contributing to the whitest [bluest] features in the representation), F555W (contributing to the yellow), and F702W (contributing to the reddest features of the depiction). Point-spread functions were matched to a common resolution of 0″.09. North is at the top, and east is at the left.

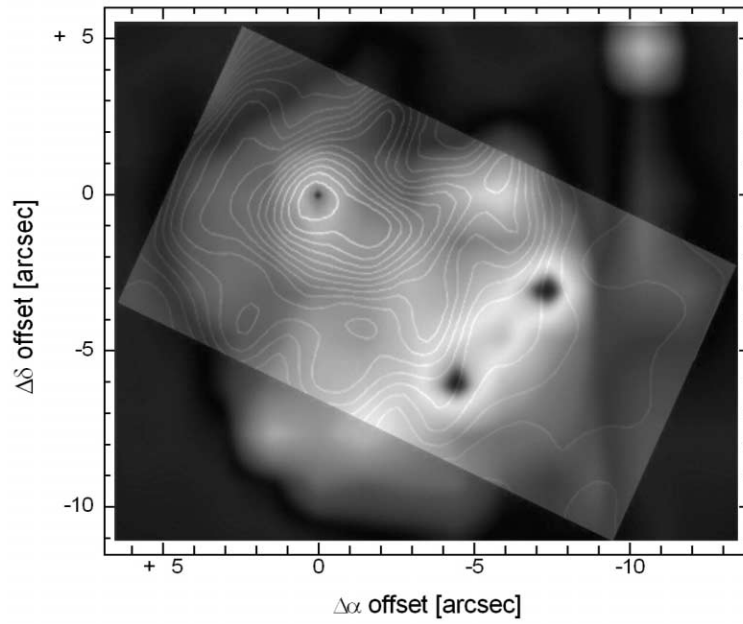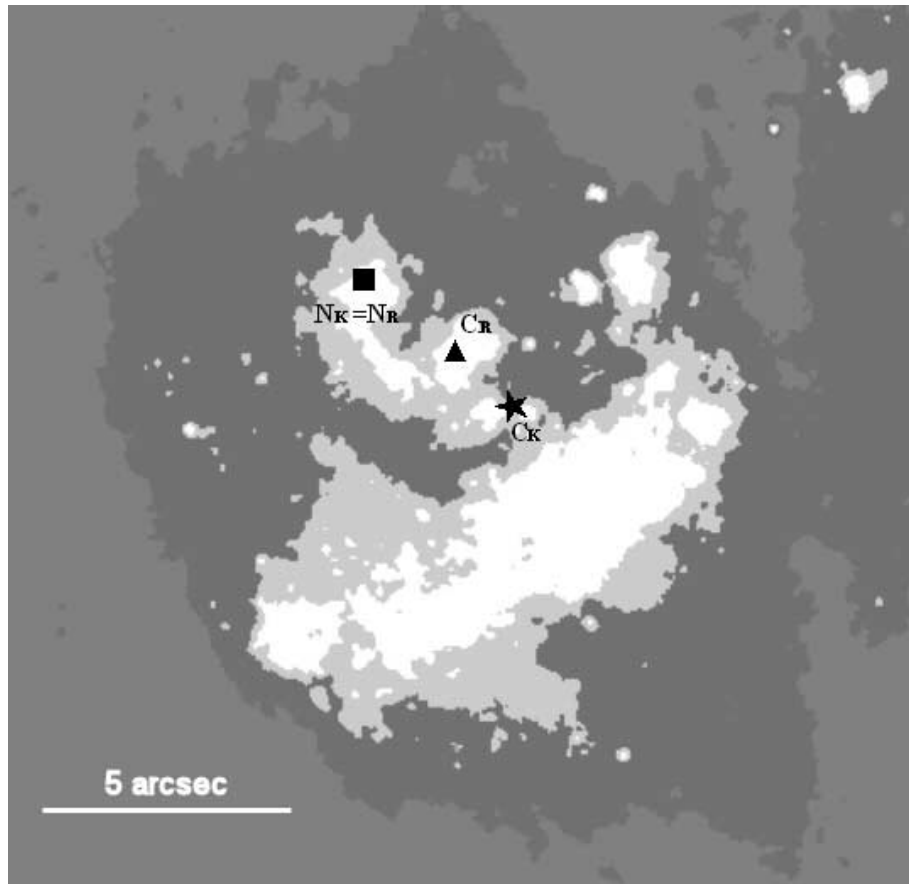Fig. 2.—Map of red continuum relative intensity (*isophotes*) computed in the range 6454–6524 Å, superposed on the F814W *HST* image smoothed to $1''$ seeing.

Fig. 3.—M83 central region. North is at the top, and east is at the left. The square marks the position of the optical nucleus, which corresponds to the continuum image peak (in the *R* band, N_R). The triangle marks the position of the red continuum symmetry center (C_R). The star marks the position of the symmetry center of the outer isophotes (bulge) in the *K*-band image (C_K).
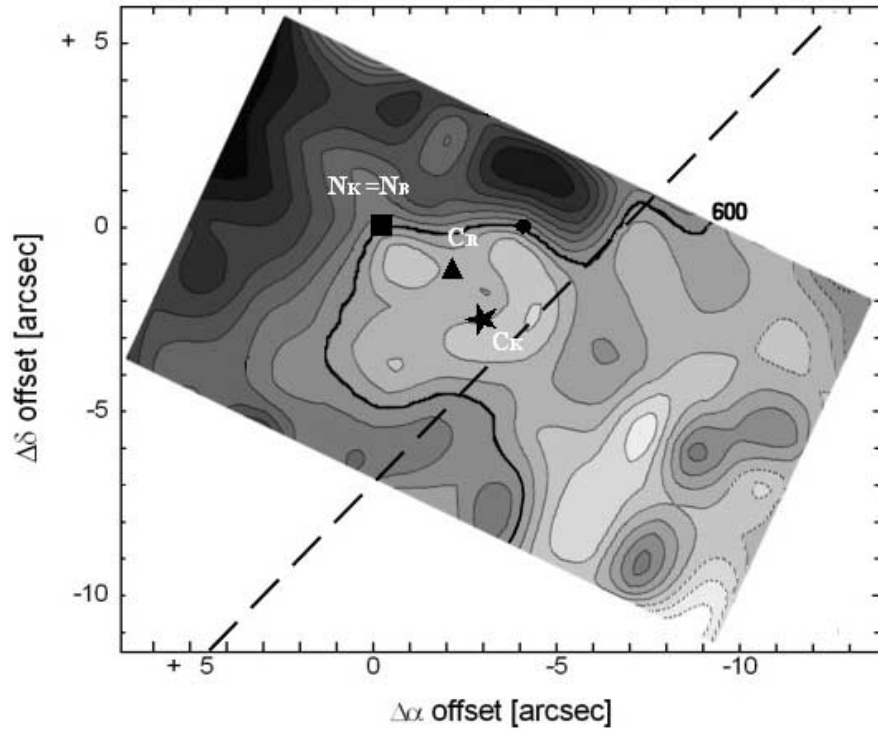
FIG. 4.—Hα radial velocity field. The square indicates the position of the optical nucleus, and the circle marks the position of the hidden mass concentration. The symbols C_R and C_K are the symmetry centers noted in Fig. 3. The isovelocities are depicted in steps of 10 km s^{-1} (2 σ uncertainty). The highest and lowest values are 634 and 542 km s^{-1}, respectively. Dark colors show blueshift, and light colors show redshift. The thicker contour corresponds to the systemic velocity. The dotted line marks the global minor axis at a P.A. of 136°. The isovelocity contours with less robust S/N-values have been marked with dotted lines.
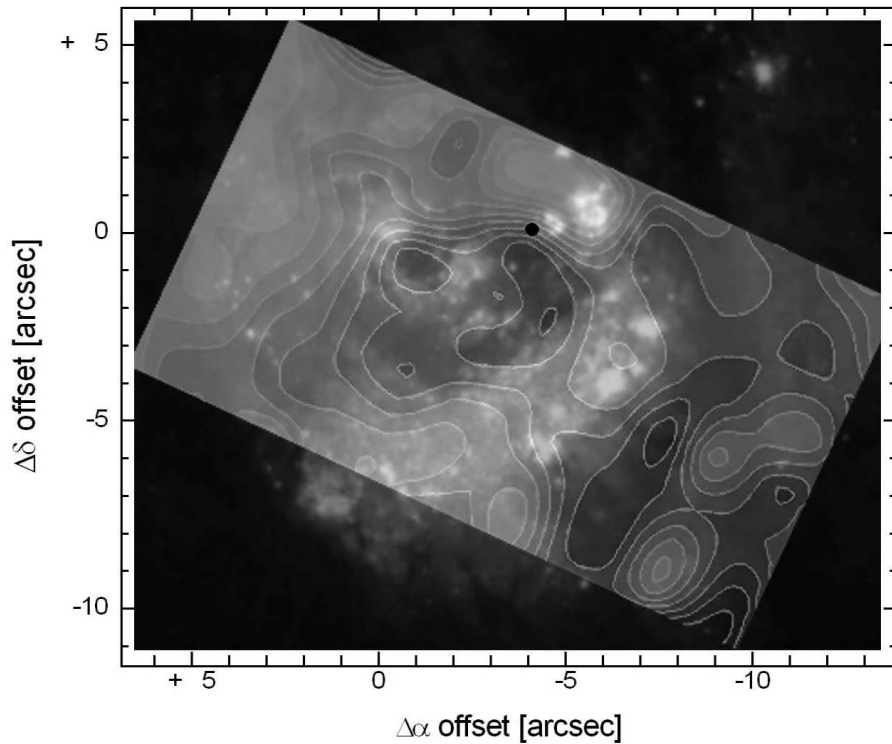
FIG. 5.—Hα radial velocity field + *HST* gray-scale image. Note the line stretching coincident with the continuum peak. The circle marks the position of the hidden mass concentration. Contour levels are the same as in Fig. 4.
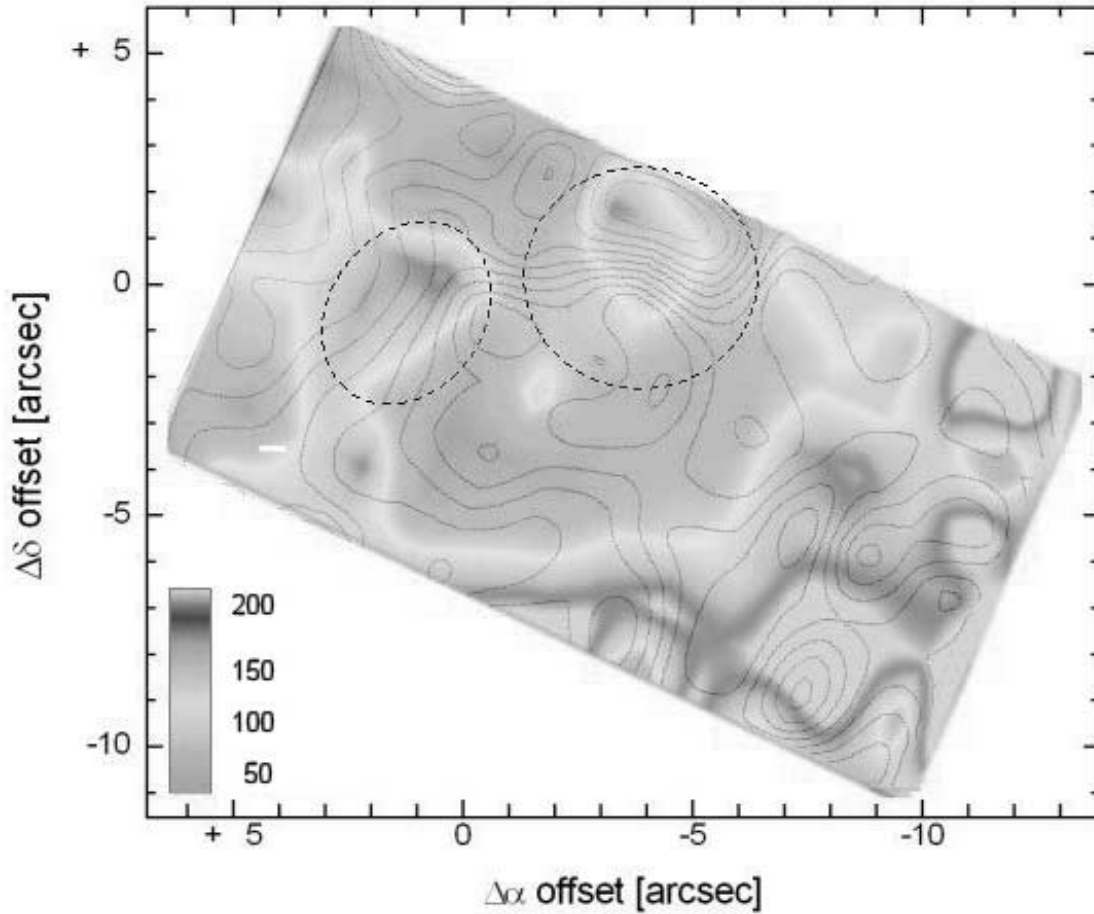
FIG. 6.—Distribution of radial velocity FWHM. The highest values are depicted as dark. The isolines correspond to the Hα velocity field. The darkest zones correspond to FWHM ∼ 200 km s^{-1}. Areas with predominant circular motion are drawn with dotted lines. In the gray zones with values below 100 km s^{-1} (*white*), the line widths are not distinct from the instrumental profile. The inset scale is in kilometers per second.

be 2″4 ± 0″5 northwest of the red continuum symmetry center. Therefore, the hidden mass concentration is 3″9 ± 0″5 from the optical nucleus (continuum emission peak), at a P.A. of 271° ± 15°. Using the astrometric parameters of the *HST* WFPC observations, we derive the position of the main nucleus: $\alpha = 13^{h}37^{m}00^{s}\!.919$, $\delta = -29°51′55″\!.66$ (J2000.0), with a 0″1 uncertainty. Assuming that this is the position of the peak continuum emission in our maps, the coordinates of the hidden nucleus would be $\alpha = 13^{h}37^{m}00^{s}\!.540 \pm 0^{s}\!.04$, $\delta = -29°51′53″\!.62 \pm 0″5$ (J2000.0), considering an uncertainty in the position of one-third of a sampling element. The position was determined from cosine fitting to the radial velocity azimuthal profiles. The uncertainty is determined by the amount of rotation center displacement that makes the fit clearly wrong. This displacement is about $d/\sqrt{n}$, where d is the sampling element size in arcseconds and n is the number of sampling elements that show a rotation pattern. The hidden nucleus is at the northwest extreme of the star formation arc. Its position can be projected on the long-slit direction of Thatte et al. (2000), and this projection is at the same position where the authors note a local maximum in the stars' velocity dispersion. The position difference is 2″5 along a direction perpendicular to the slit used by Thatte et al. (2000).

The observed region is too small on a galactic scale and is also perturbed, and in order to derive the kinematic parameters, we smoothed the observed radial velocity field with a median filter of size 6″ × 6″. The result is shown in Figure 7. The P.A. of the minor axis is 138°, very near the P.A. of the low-resolution CO

velocity field determined by Lundgren et al. (2004) of 136°. The masses can be estimated from the Keplerian approximation,

$$M \sim 233V^2R/\sin i, \qquad (1)$$

where i is the inclination, V the velocity in kilometers per second, R the radius in parsecs, and M the mass in solar masses. Therefore, we assumed for the mass estimations an inclination equal to the global inclination value of 24° (Comte 1981). The estimated masses of the nuclei within a 1″5 radius would be around $(1.2 \pm 0.2) \times 10^7 M_{\odot}$ (optical nucleus) and $(2.4 \pm 0.2) \times 10^7 M_{\odot}$ (hidden nucleus). There is no intention to report strict Keplerian rotation around the mass concentrations; we just note a predominance of circular motions involving several detection elements (lenses), and we derive upper limits for the masses in a Keplerian approximation.

In order to see if the gas is in an ordered rotation around the mass concentrations, we studied the line profiles; a strongly asymmetric line profile with pronounced wings on one side is more likely due to nongravitational motions. As can be seen in Figure 8, this is not the case for the spectra in the hidden nucleus position.

4.3. *FWHM Map*

Figure 6 shows a FWHM map with the radial velocity field superposed. Two local peaks coincident, within the uncertainties,
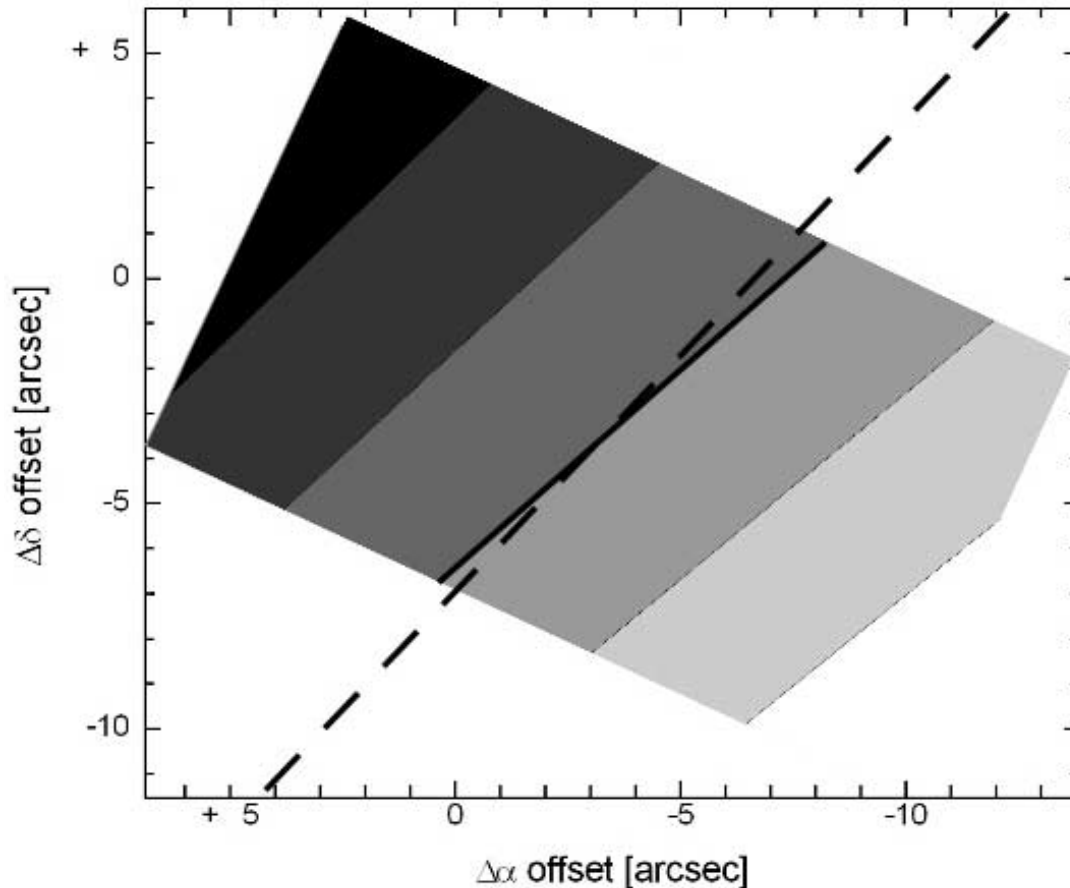
Fig. 7.—Smoothed ($6'' \times 6''$) radial velocity field. The isovelocities are depicted in steps of 20 km s^{-1}. The minor axis P.A. of the resulting smoothed field is $132°$. The thick contour marks the systemic velocity. Also drawn with the dotted line is the global CO velocity field minor axis P.A. of $136°$ (Lundgren et al. 2004).

with the position of the two mass concentrations indicated in Figure 4 can be seen. We note here that the lack of exact coincidence between the kinematic centers and the FWHM peaks could be real. This is the case for the eccentric disk of M31 (see Fig. 7 of Bacon et al. 2001), in which the lack of symmetry in the gravitational potential generates a difference in the locations of the rotation center and the observed velocity dispersion peaks at a given resolution. It is expected that the stellar rotation (not the gas rotation) around the mass center is not necessarily circular because it is subject to perturbations (such as the presence of a nearby second nucleus). In this case the radial velocity dispersion peak is not coincident with the rotation center due to the ellipticity in the orbits (Bacon et al. 2001; Tremaine 1995). Therefore, the motion is circular only in an approximate approach that allows the mass estimations.

In the southwest part of our FWHM map, profile widths exceed 200 km s^{-1}. This could be due to shocks in the ionized gas, considering that this region coincides with the star-forming arc.

4.4. [N ii] $\lambda6583$/Hα Map

Figure 9 shows the [N ii] $\lambda6583$/Hα ratio. The position of the optical nucleus is marked with a star. A ring of mean value 0.62 is noticeable around the optical nucleus, coincident with the inner ring reported by Elmegreen et al. (1998) (Fig. 10). The ratio is comparatively low in the inner ring region (nuclear region) and in the star-forming arc, ranging from values between 0.40 in the

star-forming arc to 0.46 in the inner ring region. Those values are expected for normal H ii regions (lower than 0.5; Osterbrock 1987). The peak value in the ring is $\sim$0.73 $\pm$ 0.02. Assuming that those ratios depend mainly on the abundance effects, their distribution would indicate that the relative abundance of nitrogen is higher in the ring than in the nuclear region and the star-forming arc. The low $I(6584$ Å$)$ in relation to Hα would suggest that the starburst in the nuclear region and in the star-forming arc is younger than in the ring. The values at the region of $3''$ around the hidden nucleus are $\sim$0.66 $\pm$ 0.02.

5. DISCUSSION

It is important to note that the circular motion around both regions has been measured within several detection elements. Furthermore, the local kinematics suggests that the secondary nucleus is more massive, but another possibility must be mentioned: a warp in the nuclear region could eventually mimic strong distortions of the kinematic minor axis, but the shape of the observed velocity field with two isoline stretchings would be very difficult to reproduce with a mild local change of geometric parameters and a single warp model. Other possibilities were considered, such as kinematic distortions arising in bars and spiral arms, but (1) the shape of the radial velocity field cannot be successfully compared with those resulting from numerical modeling, such as those by Piner et al. (1995) for a barred potential; and (2) we do not detect in the K band nuclear bars or spiral arms in the region of the velocity field distortion. In order to yield much
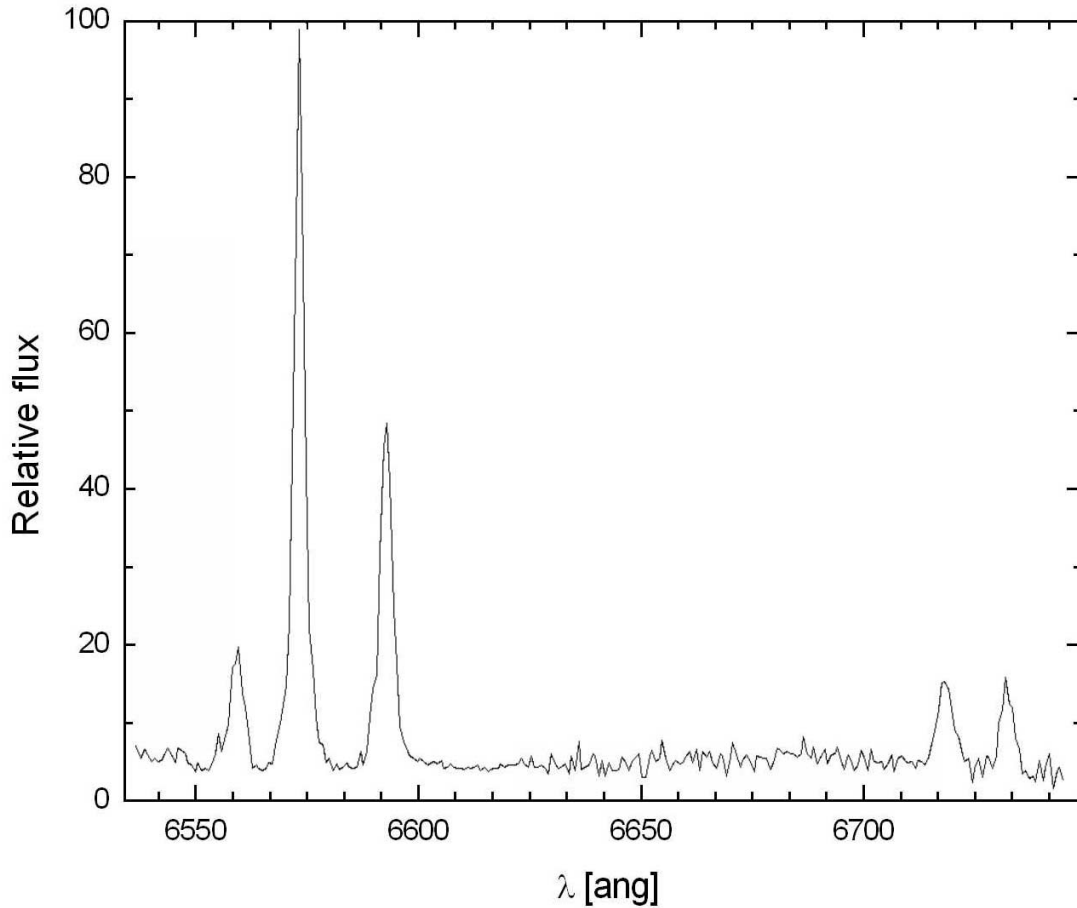
FIG. 8.—Spectra of a single sampling element from the hidden mass concentration region. Note that there are no strong asymmetries in the line profiles.

greater insight into the physics of the nuclear region, we use the Hα and Paα *HST* images, together with case B recombination theory, to construct an extinction map of the line emission from the Hα/Paα ratio (Fig. 11). This was made in the same way that Harris et al. (2001) used the Hα/Hβ ratio. Using a two-component model for the dust extinction and following Calzetti (1997), the standard definition of the color excess is

$$E(B - V)_{\mathrm{H}_a/\mathrm{H}_b} = \frac{\log(R_{\mathrm{obs}}/R_{\mathrm{int}})}{0.4[\kappa(\lambda_a) - \kappa(\lambda_b)]}, \quad (2)$$

where R_{int} and R_{obs} are the intrinsic and observed hydrogen line ratios, respectively, and $\kappa(\lambda)$ is the extinction curve, measured at the wavelength of the emission line. Using the average LMC curve and a Seaton Galactic curve (Fitzpatrick 1986) and adopting $R_{\mathrm{int}} = 0.1$ (Lilly & Hill 1987; Osterbrock 1987), we can derive the attenuation in magnitudes from

$$A_{547} = 1.79[E(B - V) - 0.06] + 3.10 \times 0.06 \approx A_V \quad (3)$$

(from eq. [2] of Harris et al. 2001), where a foreground Milky Way component [$E(B - V)_{\mathrm{MW}} = 0.06$; Schlegel et al. 1998] is assumed. According to our extinction map, the values of A_V range from 0 to nearly 7 mag at the region marked in Figure 11.

It can be seen that the strong extinction is very localized and would not play an important role in the kinematics. The position of the hidden nucleus is, within the uncertainties, coincident with a knot appearing in the K band (the hot spot labeled "region 8" in

Fig. 8 of Elmegreen et al. [1998]). This could be the IR source corresponding to the hidden mass concentration.

The Hα map, not shown here, does not clearly reveal the existence of the innermost circumnuclear ring reported by Elmegreen et al. (1998). Frequently, such rings are constituted by a discrete series of emission regions. In this case the ring is conspicuous in the near-IR color maps presented by Elmegreen et al. (1998) and in our N II/Hα map, probably suggesting different properties (mainly age) in the H II regions instead of an enhanced star formation outside this innermost ring. The most evident Hα structure is a star-forming arc that extends from the southeast to the northwest, which would be part of an outermost circumnuclear ring (Elmegreen et al. 1998). The study of abundances in H II regions in the disks of spiral galaxies has shown the existence of negative gradients with a higher abundance, with the consequence of a higher N II/Hα ratio (e.g., Pagel & Edmunds 1981; Evans 1986; Shields 1990). The observed ratio distribution in M83 could be another example of this phenomenon. Observations of the global trend and the differences between the arm, interarm, and ring regions of the barred galaxy NGC 1566 (Agüero et al. 2004; Roy & Walsh 1986) were interpreted as possibly arising at different ages of the star-forming regions.

One question arises here: If the velocity field distribution corresponds to a binary mass concentration, can the star formation be triggered by the passage of the hidden nucleus through the high-gas-density medium? It has been claimed that if a merging satellite galaxy has no nucleus (e.g., the Magellanic Clouds), the gas in the satellite will interact with the gas in the host disk and then be settled in the disk before reaching the nuclear region. On the other
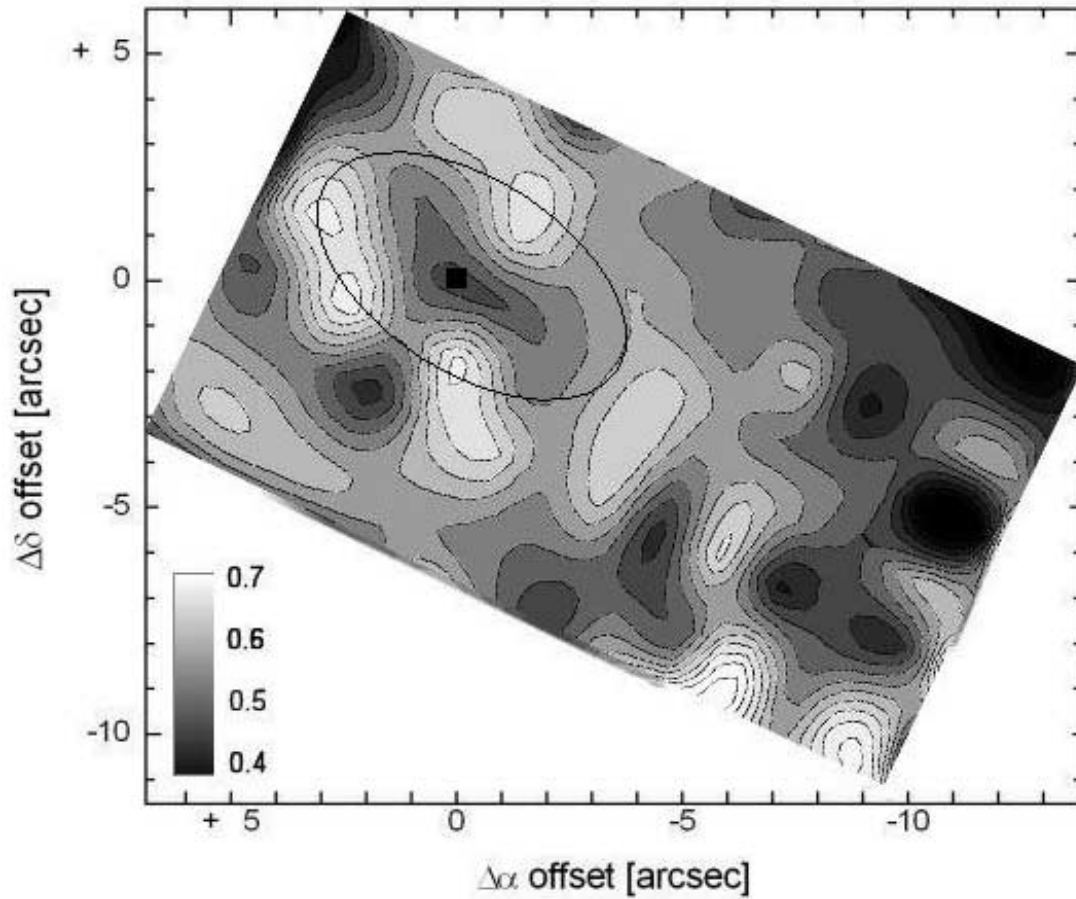
Fig. 9.—N II/Hα ratio map. The peaks of the N II/Hα ratio greater than 0.6 (*lightest in the figure*) are surrounded by a dark contour. The square marks the position of the optical nucleus.

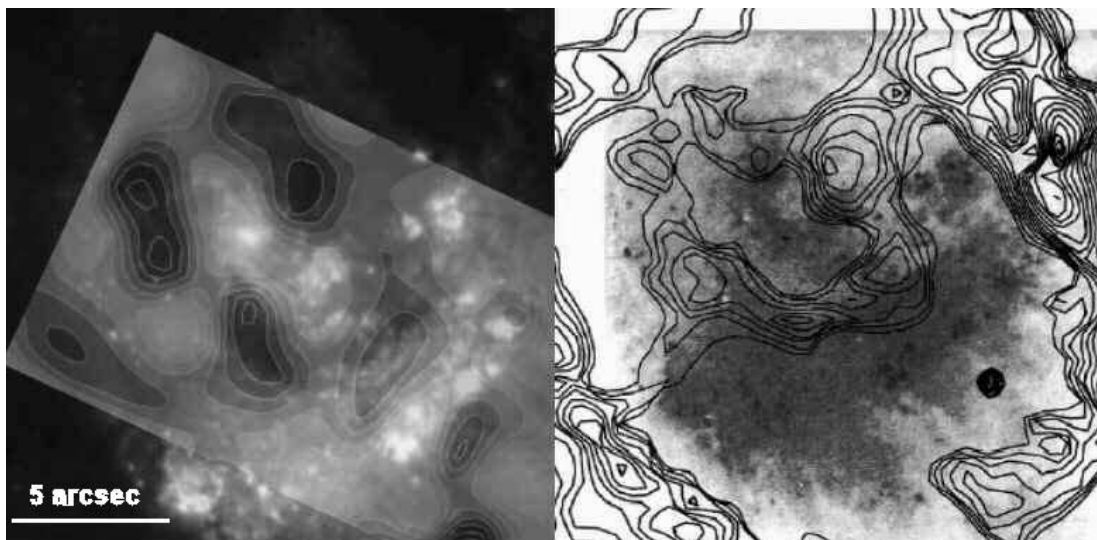Fig. 10.—*Left*: N II/Hα ratio map superposed on the gray-scale *HST* image. *Right*: $(J - K)$ unsharp-masked contours overlaid on an *HST V*-band image by Heap (1994) (Fig. 5 from Elmegreen et al. 1998).
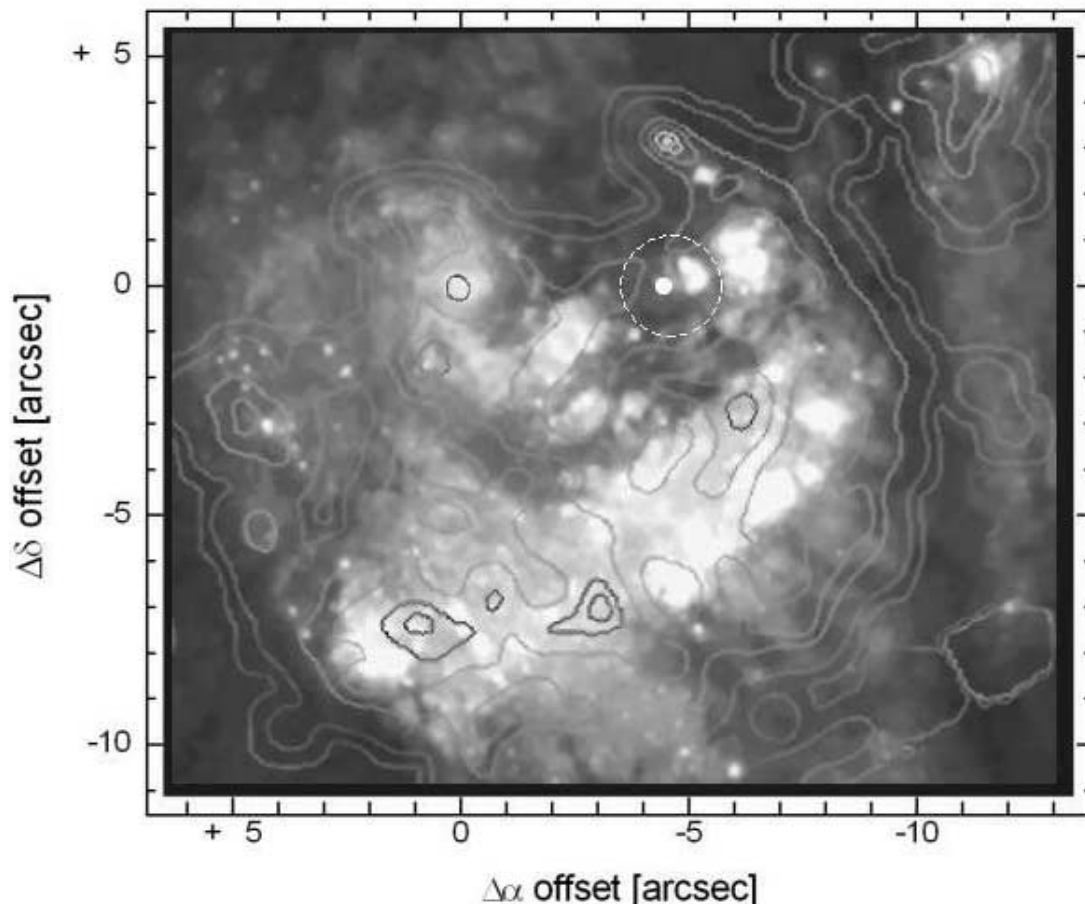
FIG. 11.—Line emission extinction map generated from the Paα/Hα *HST* images ratio (*contours*) overlaid on a gray-scale *HST* image. Contour values range from 0.15 at the optical nucleus (*dark contours*), which correspond to $A_V = 0.9$ mag, to 2.3 at $(\Delta\alpha, \Delta\delta) = (-5'', 2''5)$ (*light contours*), which correspond to $A_V = 6.8$ mag. The white circle marks the position of the hidden mass concentration, and the dotted circle marks the uncertainty in its location.

hand, if it has a nucleus (e.g., M32), the satellite nucleus will sink toward the nuclear region because of the dynamical friction (Taniguchi & Wada 1996). It is assumed that a nucleus is either a supermassive black hole or a significant concentration of nuclear star clusters. In this respect, satellite galaxies in Mihos & Hernquist (1994) and Hernquist & Mihos (1995) are also nucleated ones. The formation mechanism of the corresponding nuclear starburst and hot-spot nucleus would involve a supermassive binary of compact objects formed by a merger with a nucleated satellite galaxy, triggering intense star formation in the central regions of the main spiral galaxy, in which the nuclear gas disk has been formed already by the dynamical effect of the merger itself. As the secondary compact object approaches the nuclear gas disk, the gas disk responds to the gravitational perturbation caused by the nonaxisymmetric potential of the binary mass, forming asymmetrical spiral patterns. When the mass of the intruding object is only 1/10 of the primary's, the gas response is so mild that only pseudoring features or tightly wound spiral arms are formed in the circumnuclear region. These features are expected to evolve into several H II region clumps, leading to the formation of not-very-bright hot-spot nuclei. On the other hand, when the mass of the intruding nucleus is comparable to half the primary one, a very strong one-arm spiral shock appears after the close passage of the secondary in each orbital period. The gas clouds are forced to move rapidly into the central region owing to frequent collisions of gas clouds, and the starburst is triggered near the nucleus. If this were the case, then the age gradient in the

star-forming arc (see § 1) that ends in the hidden nucleus would provide the clue to the dynamical evolution of this complex system.

6. CONCLUSIONS

In this work we studied the morphology, the ionized gas emission, and the kinematics in the innermost regions of M83. A hidden nucleus is not evident in the *HST* images, although kinematically the radial velocity field points out the presence of a strong mass concentration that could be the mentioned nucleus. Its condition of being nondetectable could be due to its location, considering that the kinematically derived position lies close to a strong absorption region ($A_V \sim 7$ mag; see Fig. 11).

The [N II] emission of the hidden nucleus region is relatively low compared with the Hα emission. According to previous works, this could be the younger end of the star-forming arc. This could be consistent with lower metallicity, but the lack of more emission-line ratios precludes a direct confirmation with the data presented here. Notwithstanding, two independent works confirmed through photometry (Harris et al. 2001) the age gradient of this star-forming arc. The emission-line ratio map also unveils the presence of a second circumnuclear ring structure, previously discovered by IR imaging (Elmegreen et al. 1998).

Using the Keplerian approximation, the optical nucleus would have a mass of $(5.0 \pm 0.8) \times 10^6 \, M_\odot / \sin i \, (r < 1''5)$, and the secondary nucleus, located $4'' \pm 1''$ to the northwest (P.A. of $271° \pm 15°$) of the optical nucleus, would have a mass of

$(1.00 \pm 0.08) \times 10^7 \ M_\odot/\sin i$ ($r < 1''5$). The FWHM map presents local maxima in the nuclei positions, supporting the conclusion about the presence of two central mass concentrations derived from the radial velocity map.

The behavior of the interstellar medium inside the circumnuclear ring and around the binary mass concentration has been resolved. The hidden nucleus is located at the younger end of the giant arc of star formation, suggesting that the local departure of an axisymmetric gravitational potential would be the trigger of the nuclear starburst in M83.

REFERENCES

Agüero, E. L., Díaz, R. J., & Bajaja, E. 2004, A&A, 414, 453
Arribas, S., & Mediavilla, E. 1994, ApJ, 437, 149
Bacon, R., Emsellem, E., Combes, F., Copin, V., Monet, G., & Martin, P. 2001, A&A, 371, 409
Boulesteix, J. 1993, ADHOC Reference Manual (Marseille: Pub. Obs. Marseille)
Calzetti, D. 1997, AJ, 113, 162
Comte, G. 1981, A&AS, 44, 441
de Vaucouleurs, G., de Vaucouleurs, A., Corwin, H., Jr., Buta, R., Paturel, G., & Fouque, P. 1991, Third Reference Catalogue of Bright Galaxies (New York: Springer)
Díaz, R., Dottori, H., Carranza, G., & Goldes, G. 1999, ApJ, 512, 623
Díaz, R., Dottori, H., Vera-Villamizar, N., & Carranza, G. 2003, ApJ, 597, 860
Díaz, R., Paolantonio, S., Goldes, G., & Carranza, G. 1997, Multifunctional Integral Field Spectrograph (Cordoba: Natl. Univ. Cordoba)
Elmegreen, D., Chromey, F., & Warren, A. 1998, AJ, 116, 2834
Evans, I. N. 1986, ApJ, 309, 544
Fitzpatrick, E. 1986, AJ, 92, 1068
Gallais, P., Rouan, P., Lacombe, D., Tiphene, D., & Vauglin, L. 1991, A&A, 243, 309
Harris, J., Calzetti, D., Gallagher, J., Conselice, C., & Smith, D. 2001, AJ, 122, 3046
Heap, S. 1994, in Violent Star Formation: From 30 Dor to QSOs, ed. G. Tenorio-Tagle (Cambridge: Cambridge Univ. Press), 303
Heap, S., Holbrook, J., Malumuth, E., Shore, S., & Waller, W. 1993, BAAS, 182, 3104
Hernquist, L., & Mihos, C. 1995, ApJ, 448, 41
Lilly, S. J., & Hill, G. J. 1987, ApJ, 315, L103
Lundgren, A., Olofsson, H., Wiklind, T., & Rydbeck, G. 2004, A&A, 422, 865
Mast, D. 2002, M.S. thesis, Natl. Univ. Córdoba
Mast, D., Díaz, R., Agüero, M. P., Weidmann, W., Carranza, G., & Gimeno, G. 2002, Bull. Asoc. Argentina Astron., 45, 74
Mihos, C., & Hernquist, L. 1994, ApJ, 425, L13
Oddone, M. A., Goldes, G., Carranza, G., Díaz, R., Plana, H., & Boulesteix, J. 1999, Bull. Asoc. Argentina Astron., 43, 70
Osterbrock, D. E. 1987, Astrophysics of Gaseous Nebulae and Active Galactic Nuclei (Mill Valley: University Science Books)
Pagel, B. E. J., & Edmunds, M. G. 1981, ARA&A, 19, 77
Piner, G., Stone, J., & Teuben, P. 1995, ApJ, 449, 508
Roy, J., & Walsh, J. 1986, MNRAS, 223, 39
Schlegel, D. J., Finkbeiner, D. P., & Davis, M. 1998, ApJ, 500, 525
Shields, G. A. 1990, ARA&A, 28, 525
Soria, R., & Wu, K. 2003, A&A, 410, 53
Taniguchi, Y., & Wada, K. 1996, ApJ, 469, 581
Thatte, N., Tecza, M., & Genzel, R. 2000, A&A, 364, L47
Tremaine, S. 1995, AJ, 110, 628
Vega, L. 2000, M.S. thesis, Natl. Univ. Córdoba
Vega, L., Díaz, R. J., Lípari, S., Storchi-Bergmann, T., & Dottori, H. 2000, Bull. Asoc. Argentina Astron., 44, 68